CrossMark

ORIGINAL PAPER

Mesoporous silica materials functionalized with folic acid: preparation, characterization and release profile study with methotrexate

Luiza Baptista de Oliveira Freitas[1] · **Ismael José Gonzalez Bravo**[1] ·
Waldemar Augusto de Almeida Macedo[1] · **Edésia Martins Barros de Sousa**[1]

Abstract Ordered mesoporous silica materials exhibit potential features to be used as controlled drug delivery systems, including biocompatibility, textural and structural properties. In this paper, ordered mesoporous materials SBA-15, SBA-16 and MCM-41, which present different morphologies, pore sizes and array of mesopores (2D hexagonal, 3D cubic and 2D hexagonal, respectively), were synthesized, functionalized with folic acid by post-synthesis grafting and loaded with the anticancer agent methotrexate. The drug loading and its release kinetics profile were compared between all materials. The mesoporous silicas were characterized through thermogravimetric analysis, CHN elemental analysis, Fourier transform infrared spectroscopy, small-angle X-ray scattering, N_2 adsorption, zeta potential, scanning electron microscopy and transmission electron microscopy in order to evaluate their physical–chemical properties. The interactions between methotrexate and the materials' surface were systematically evaluated using X-ray photoelectron spectroscopy. The results showed the drug release kinetic might be controlled by the synthesis procedure and the degree of surface functionalization of the mesoporous silica.

Graphical Abstract
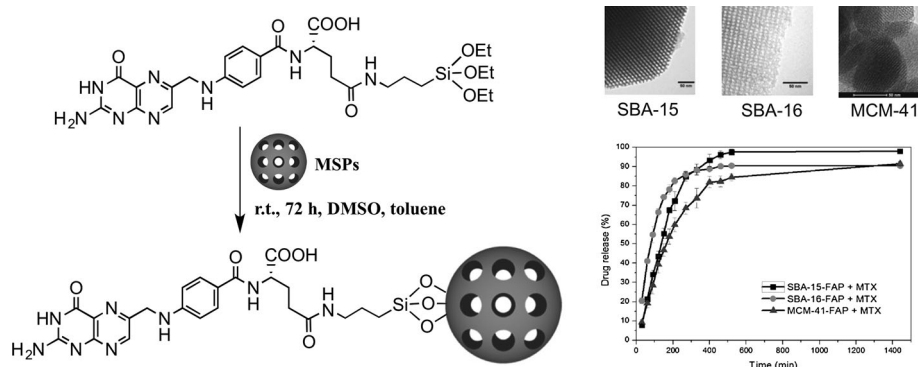
✉ Edésia Martins Barros de Sousa
sousaem@cdtn.br

[1] Laboratório de Materiais Nanoestruturados para Bioaplicações, Comissão Nacional de Energia Nuclear – Centro de Desenvolvimento da Tecnologia Nuclear – (CNEN/CDTN), Av. Presidente Antônio Carlos 6.627, Pampulha, Belo Horizonte, MG 31270-901, Brazil

1 Introduction

Drug delivery systems have been applied to prolong the circulation time and bioavailability of certain drug molecules, and addressing the drug delivery vehicles to specific tissues or cells [1, 2]. It allows the carrier of drugs that have

limited use due to low solubility, high toxicity, in vivo instability, lack of specificity in the therapeutic target and low bioavailability [3]. One of the major goals of these systems is to provide more effective treatment regimens by reducing drug dosing frequency and improving safety [4–6].

Mesoporous silica particles (MSPs) possess several advantages as drug delivery carriers due to their specific features such as: the ordered pore network with homogeneous size, that allows a high control of the drug loading and the release kinetics profile; uniform and tunable size and shape of the particles; high pore volume and surface area that allow a high drug load and drug adsorption; non-toxicity and biocompatibility [4–8]. In addition, the presence of free silanol groups on the surface of these materials allows their functionalization with a wide variety of molecules. As a result, the chemically modified MSPs acquire new properties that may offer targeted delivery, controlled release, improved bioavailability and cellular uptake [5, 9–11]. Together, these parameters may strongly influence the drug loading, the pharmacokinetic release profiles and their interaction with cells, tissues or molecules, making the modified MSPs very attractive for a number of applications in both nanomedicine and biotechnology [5, 12–14].

The functionalization process taken by post-synthesis grafting of organosilane precursors is widely used because it is a straightforward method that provides the anchorage of different molecules or functional groups to the MSPs' surface, while maintaining its bulk material properties [4, 15]. For example, the functionalization of MSPs with ligands that are recognized by specific cellular receptor has been shown to impact the uptake efficiency and their route of entry into cells, such as by specific bindings with receptors, instead through clathrin-dependent endocytosis mechanism or pinocytosis [3, 4, 16].

In this study, MSPs with different morphologies were functionalized with folic acid (FA). FA (Fig. 1a) was chosen as a targeting agent since its receptor is overexpressed in several human tumors, including ovarian, endometrial, colorectal, breast, lung, renal cell carcinoma and breast cancers, and they are rarely expressed in normal tissues [13, 17–21]. The use of FA as a targeting ligand for selective drug delivery has emerged due to this difference in expression between normal and cancer cells. In fact, the use of folate-tagged MSPs has proven to enhance the uptake by tumor cells that overexpress the FA receptor [18–20, 22].

Methotrexate (MTX) is a folic acid derivative that is used as an allosteric inhibitor of dihydrofolate reductase (DHFR), the enzyme that catalyzes the conversion of dihydrofolate to tetrahydrofolate (Fig. 1b). Since tetrahydrofolate is required for purine and pyrimidine synthesis, methotrexate treatment results in the inhibition of DNA and RNA synthesis [12]. This anticancer agent is widely used to treat various neoplastic diseases such as acute lymphocytic leukemia, osteosarcoma and solid cancers and autoimmune diseases such as psoriasis and rheumatoid arthritis [23–26]. It is assumed that the controlled and specific MTX delivery using MSPs could maintain drug levels in the desired range, increase patient compliance and prevent the side effects of this drug which is very toxic [12].

In the present work, the mesoporous silica SBA-15, SBA-16 and MCM-41 were synthesized and functionalized with FA to afford potential delivery systems for MTX. The two-dimensional mesoporous silica MCM-41 and SBA-15 possess a hexagonal array of ordered mesopores, formed by parallel channels that can be accessible in one direction [27]. On the other hand, the three-dimensional mesoporous silica SBA-16 has a cubic array of mesopores that possesses a body-centered cubic symmetry of pores, formed by a 3D cage-like system of interconnected pores [28], which provides easy accessibility and diffusion of drugs in all directions.

Despite many years of experimental synthesis and characterization of functionalized mesoporous silica [2–4, 6, 10, 11, 13, 29], cubic mesoporous silica SBA-16 has not been studied extensively when compared to MCM-41 and SBA-15 matrices as a platform for bioapplication. As far as we know, no study describes the functionalization of SBA-16 with folate groups and only concise investigation of the chemical interactions between the adsorbed drug and the materials' surface using XPS is described for these systems [30–34]. Therefore, the main goal of this study is to evaluate the differences between SBA-15, SBA-16 and MCM-41 over the functionalization rate with folate groups, MTX loading and release profiles. Incorporation of this anticancer drug into bare MCM-41 and SBA-15 matrices was already shown [12, 25, 35], but it has never been studied with these matrices functionalized with a targeting agent. In addition, to the best of our knowledge, the load of MTX

Fig. 1 Chemical structure of folic acid (**a**) and methotrexate (**b**)
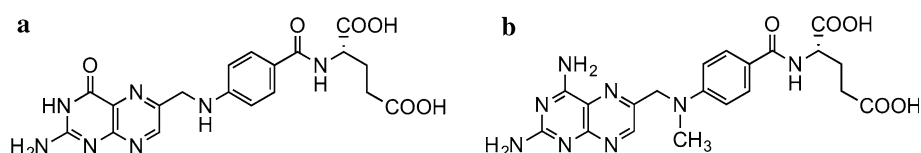
into a SBA-16 matrix has never been reported, and there are only few studies comparing the efficiency of drug loading and drug release kinetics between different mesoporous silicas using the same experimental conditions [12, 36–38].

2 Materials and methods

2.1 Materials

Dimethyl sulfoxide (DMSO), (3-aminopropyl)triethoxysilane (APTES), tetraethyl orthosilicate (TEOS), folic acid (FA), Pluronic F127 [poly(ethylene oxide)-block-poly(propylene oxide)-blockpoly(ethylene oxide), M_{av} = 12,600], Pluronic P123 [poly(ethylene glycol)-block-poly(propylene glycol)-blockpoly (ethylene glycol), M_{av} = 5800], hexadecyltrimethylammonium bromide (CTAB), methotrexate (MTX), N-hydroxysuccinimide (NHS) and 1-(3-dimethylaminopropyl)-3-ethylcarbodiimide hydrochloride (EDC·HCl) were purchased from Sigma-Aldrich (São Paulo, Brazil).

2.2 Synthesis of mesoporous silica SBA-15

SBA-15 was synthesized in accordance with the published procedure [39] using Pluronic P123 as a template in acidic conditions. In a typical experiment, the triblock copolymer Pluronic P123 (4.0 g) was dissolved in 138 mL of water and 10.3 mL of HCl (37 wt% solution) under stirring at 40 °C, until complete dissolution of the surfactant. After 1 h, TEOS (8.8 mL) was slowly added to the solution. The mixture was maintained at 40 °C for 24 h, then for 1 day at 100 °C under static conditions in a Teflon-lined autoclave. The obtained material was filtered and dried at 60 °C, and the surfactant was removed by calcination, which was carried out by increasing the temperature to 550 °C under nitrogen flow for 2 h followed by 3 h in air.

2.3 Synthesis of mesoporous silica SBA-16

SBA-16 silica was prepared with a methodology adapted [40], using commercial Pluronic F127 as a template agent in acidic conditions and n-butanol as co-surfactant. In a modified preparation, Pluronic P127 (3.0 g) was dissolved in 430 mL of water and 14 mL of 38 % HCl solution, under constant stirring, at room temperature. After approximately 30 min, 11 mL of n-butanol was added and left under stirring for 1 h. Then, 15 mL of TEOS was slowly added to the solution under constant stirring at 45 °C for 2 h. After decanting for 24 h, the solid was filtered off and dried at 60 °C for 24 h. The surfactant was removed by calcination, which was carried out by increasing the temperature to 550 °C under nitrogen flow for 2 h followed by 3 h in air.

2.4 Synthesis of mesoporous silica MCM-41

MCM-41 silica was prepared in accordance with a published procedure [18], using commercial CTAB as a template agent in basic conditions. CTAB (1.00 g, 2.74 mmol) and NaOH (280 mg, 7.00 mmol) were dissolved in 480 mL of water. The temperature of the mixture was adjusted to 75 °C. TEOS (5.00 mL, 22.4 mmol) was added dropwise to the surfactant solution under vigorous stirring. The mixture was allowed to react for 2 h to give rise to a white precipitate, which was filtered, washed with water and methanol, and dried at 60 °C for 24 h. The surfactant was removed by calcination, which was carried out by increasing the temperature to 550 °C under nitrogen flow for 2 h followed by 3 h in air.

2.5 Functionalization of mesoporous silica SBA-15, SBA-16 and MCM-41

The functionalization process was done using a methodology adapted [20]. To a 50-mL round-bottom flask covered with aluminum foil, were added DMSO (9 mL), folic acid (300 mg, 0.83 mmol), NHS (90 mg, 0.78 mmol), EDC·HCl (150 mg, 0.78 mmol) and APTES (200 μL, 0.83 mmol). After 6 h under vigorous stirring, toluene (12 mL) and the MSPs (150 mg) were added to the APTES-FA solution. The mixture was then stirred for 72 h at room temperature. The materials were recovered by filtration, and washed thoroughly with toluene, DMSO, water and acetone.

2.6 Drug loading

To load MTX, 100 mg of each type of mesoporous material was mixed with 20 mL of MTX aqueous solution (1.0 mg/mL) and kept under magnetic stirring at room temperature for 24 h. The obtained mixture was filtered, and the resulting solid was dried at 37 °C for 3 days. Elemental analysis was carried out to quantify the drug loaded inside the MSNs.

2.7 Release test

A suspension of MSPs loaded with MTX (15 mg) in simulated body fluid (SBF) (1.5 mL, pH 7.3) was put into a dialysis tube (cutoff Mn = 3500) and then placed in a flask with 38.5 mL of SBF, at 37 °C, under continuous stirring at a rate of 50 rpm. At particular time intervals, the amount of MTX released from MSPs was calculated by measuring

the absorbance at 303 nm with a UV–Vis spectrometer (Shimadzu UV–VIS V-24001). The in vitro experiments were carried out in triplicate.

2.8 Physicochemical and morphological characterization of free SBA-15, SBA-16, MCM-41 and the functionalized systems

The samples were characterized by CHN elemental analysis, thermogravimetric analysis (TGA), Fourier transform infrared spectroscopy (FTIR), small-angle X-ray scattering (SAXS), N_2 adsorption, zeta potential, X-ray photoelectron spectroscopy (XPS), scanning electron microscopy (SEM) and transmission electron microscopy (TEM) techniques.

The functionalization rate and drug-loading rate were determined by elemental analysis, which were performed in a Perkin-Elmer CHNS model 2400. The weight loss of the samples was determined in a Shimadzu thermogravimetric analyzer (TGA) 50WS. All measurements were carried out within a nitrogen atmosphere (20 mL/min) using a sample mass of approximately 4 mg from 20 to 750 °C, in a temperature rate of 5 °C/min. The typical functional groups from silica and from the functionalizing agents were characterized by FTIR. The procedure was conducted in a Thermo Nicolet 6700 spectrophotometer, ranging from 4000 to 400 cm^{-1} with 64 scans and 4 cm^{-1} of resolution. Zeta potential was measured using Zetasizer Nano ZS (Malvern Instruments, Malvern, UK). For the analysis, an aqueous dispersion of nanoparticles (0.05 mg/mL) was prepared. After sonication of the suspension for 5 min, the measurements were made in triplicate. Nitrogen adsorption isotherms of samples were obtained using a Quantachrome Nova 2200 adsorption analyzer. Before the adsorption measurements, non-functionalized materials were outgassed for 4 h at 300 °C, whereas the functionalized ones were outgassed for 48 h at 40 °C. All data analyses were performed using the NovaWin V.10, 1997–2007 Quantachrome Instruments software (Boynton Beach, FL, USA). The specific surface areas were determined by the Brunauer–Emmett–Teller (BET) method at −196 °C, according to the manufacturer's instructions. The SAXS patterns were obtained using Ultima IV® (Rigaku). The incident X-ray was set at 1.54 Å wavelength, and the angle scattering (2θ) in the range 0°–2° or 0°–6°. The XPS analysis was performed using a Specs surface analysis system equipped with a Phoibos 150 electron analyzer and a monochromatized Al K_α radiation (1486.6 eV) at a power of 350 W. An electron flood gun operated at 0.1 μA was used to compensate the charge effect in the samples, and the C 1s signal (284.6 eV) was employed as reference for the calibration of the binding energies (BE) of different elements. The CasaXPS software was used to process the data analysis and to estimate the samples surface composition. Morphological characterization was performed using the scanning electron microscope (SEM—Quanta 200-FEG-FEI-2006 or FE-SEM Sigma VC—field emission) operating at 30 kV and a transmission electron microscope (TEM—Tecnai-G2-20-FEI 2006) at 200 kV of the Microscopy Center of UFMG, Belo Horizonte, Brazil.

3 Results and discussion

3.1 SEM microscopy

The particles morphology and size were measured by scanning electron microscopy (SEM). SEM images of the SBA-15, SBA-16 and MCM-41 samples are compared in Fig. 2. The image shows that SBA-15 has a rod-like morphology, with an average length of 2.2 μm and 0.7 μm of width. The SBA-15 particles presented aggregated macrostructures. SBA-16 synthesis led to a mixture of cubic, faceted and spherical particles with diameters around 5.0 μm. The MCM-41 particles presented homogeneous spherical morphology, with an average diameter of 110 nm.

3.2 TEM microscopy

The ordered pore structure of SBA-15, SBA-16 and MCM-41 was verified by transmission electron microscopy
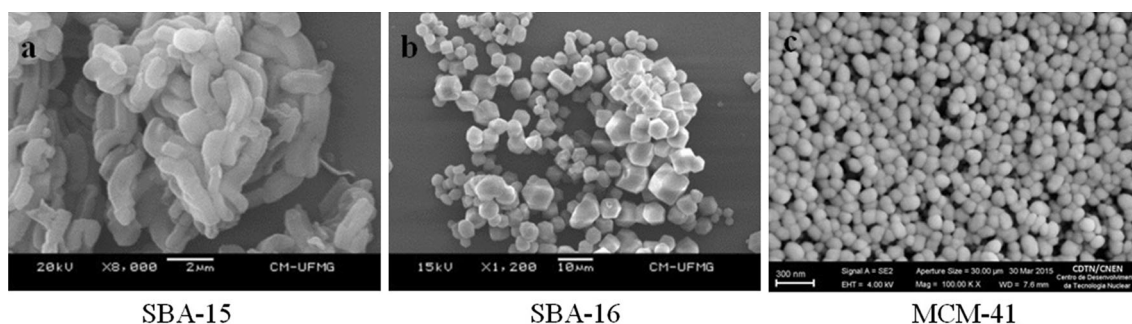

Fig. 2 SEM images of SBA-15 (**a**), SBA-16 (**b**) and MCM-41 (**c**) samples

(TEM). TEM images of these matrices are compared in Fig. 3. The images show that SBA-15, SBA-16 and MCM-41 materials are highly porous and their pore diameters measured from the images are about 6.4, 3.5 and 2.4 nm, respectively.

The periodical, well-organized hexagonal array of mesopores of SBA-15 and MCM-41 are shown and corroborate to the 2D structure of these materials. The micrographs of SBA-15 and MCM-41 particles show a channel structure of the mesopores with parallel stripes (Fig. 3a and c, respectively) and hexagonally packed light dots (Fig. 3a′ and c′, respectively) when the electron beam was perpendicular to the main axis [27]. The images of SBA-16 showed unidirectional pore channels when the

electron bean was perpendicular to the channel axis of the mesopores (Fig. 3b), and presented cubic arranged and uniform pore arrays, when the incident electron beam was parallel to the main axis of the mesopores (Fig. 3b′) [10, 41]. Thus, the TEM investigation offers consistent evidence that the ordered structure is obtained in the approach employed in this work.

3.3 Functionalization

The functionalization of SBA-15, SBA-16 and MCM-41 with FA was achieved by a two-step, one-pot reaction using a methodology adapted from Lu et al. [20]. First, FA
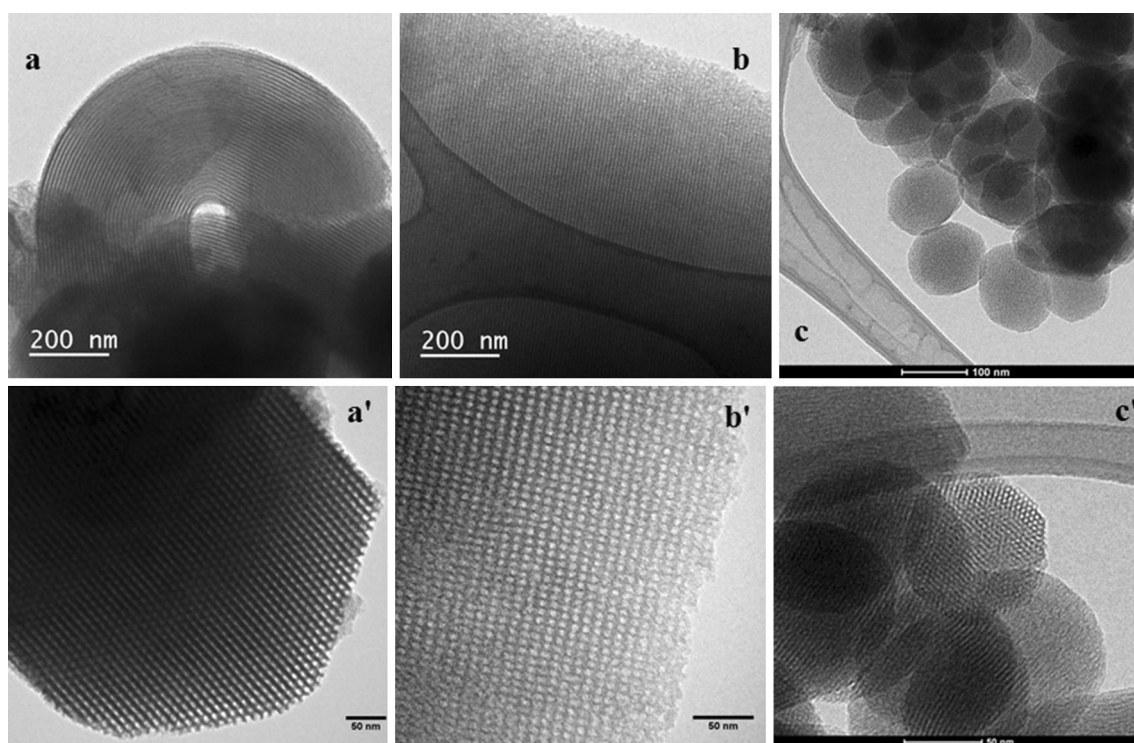

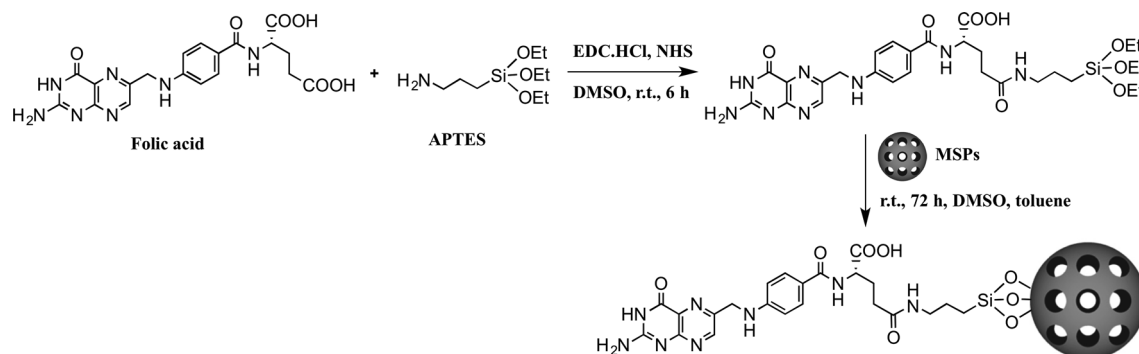Fig. 3 TEM images of SBA-15 (a), SBA-16 (b) and MCM-41 (c) samples

Fig. 4 Functionalization process of MSPs with folic acid targeting ligand

was linked to APTES, the trialkoxysilane silane source, through an amide group using the coupling reagent EDC·HCl and NHS as a catalyst. Next, the bare MSPs were added to the mixture of APTES-FA to promote the silanization of the silica surface (Fig. 4). The degree of functionalization of these silica matrices with the functional group N-folate-3-aminopropyl (FAP) will be discussed in the following topics.

3.4 CHN elemental analysis

The CHN analysis of bare SBA-15, SBA-16 and MCM-41 matrices and the functionalized ones was used to quantify the organic molecules anchored to its surfaces. The results are shown in Table 1. The carbon and nitrogen concentrations of MSPs-FAP increased significantly in relation to the bare MSPs, indicating that the bare matrices were successfully functionalized with FAP. The degree of functionalization of SBA-15 with APTES-FA (15.3 % of C) was higher than it was for SBA-16 (8.7 % of C), which was higher than for MCM-41 (6.6 % of C).

The elemental analysis was also used to quantify the amount of MTX incorporated into the mesoporous materials. Regarding the bare MSPs, there was no significant difference between the drug loading, since the percentage composition of C was 6.4, 6.5 and 5.6 % for SBA-15, SBA-16 and MCM-41, respectively. On the other hand, when compared the rate of MTX loaded into the functionalized MSPs, the less functionalized silica, MCM-41-FAP, showed a higher value of drug loading (6.0 % C), while SBA-15-FAP and SBA-16-FAP presented lower values (5.1 and 5.3 % C, respectively).

3.5 Thermogravimetric analysis (TGA)

The thermogravimetric analysis was also used to infer the degree of functionalization and the amount of drug loaded into the mesoporous materials. TGA curves of all systems are shown in Fig. 5, and the percentages of weight loss are shown in Table 2. The three unmodified MSPs showed two distinct weight loss regions. The first region of mass loss (about 7.6–12.6 %) occurs in temperature range between 20 and 150 °C, which could be attributed to the thermodesorption of physically adsorbed water from the silica surface. The second region, in the temperature range from 150 to 650 °C, the TGA curve is relatively flat. The weight loss in this second region is almost negligible (from 1.8 to 3.8 %) and corresponds to the silanol condensation [42]. As a result, all the bare MSPs showed excellent thermal stability in the investigated temperature range.

The TGA curves of the functionalized and/or drug-loaded MSPs differ significantly from those of bare silica matrices. The first region of weight loss corresponds to the thermodesorption of physically adsorbed water, which varies according to the sample. The samples that show a decreased value of weight loss in this region indicates an increasing hydrophobic character of the material and a decrease in the effective silanol concentration [43]. The weight loss between 150 and 750 °C indicates the decomposition of the incorporated organic material (FAP and/or MTX). The larger the percentage of mass loss, the higher is the degree of functionalization with FAP or the incorporation of MTX.

The TGA curves of MSPs-FAP should present four characteristic stages of FA melting with simultaneous decomposition [44, 45], but they are overlapped. The thermal decomposition data confirm the presence of functionalized groups in all matrices, since there is no significant weight loss in the parent MSPs within this same temperature range. Similarly to elemental analysis, the TGA curves showed a higher degree of functionalization with FAP to SBA-15 (24.1 % w/w) than to SBA-16 (20.6 % w/w), which was higher than it was to MCM-41 (7.7 % w/w). In addition, the TGA analysis

Table 1 Elemental analysis of SBA-15, SBA-16, MCM-41 and its functionalized samples

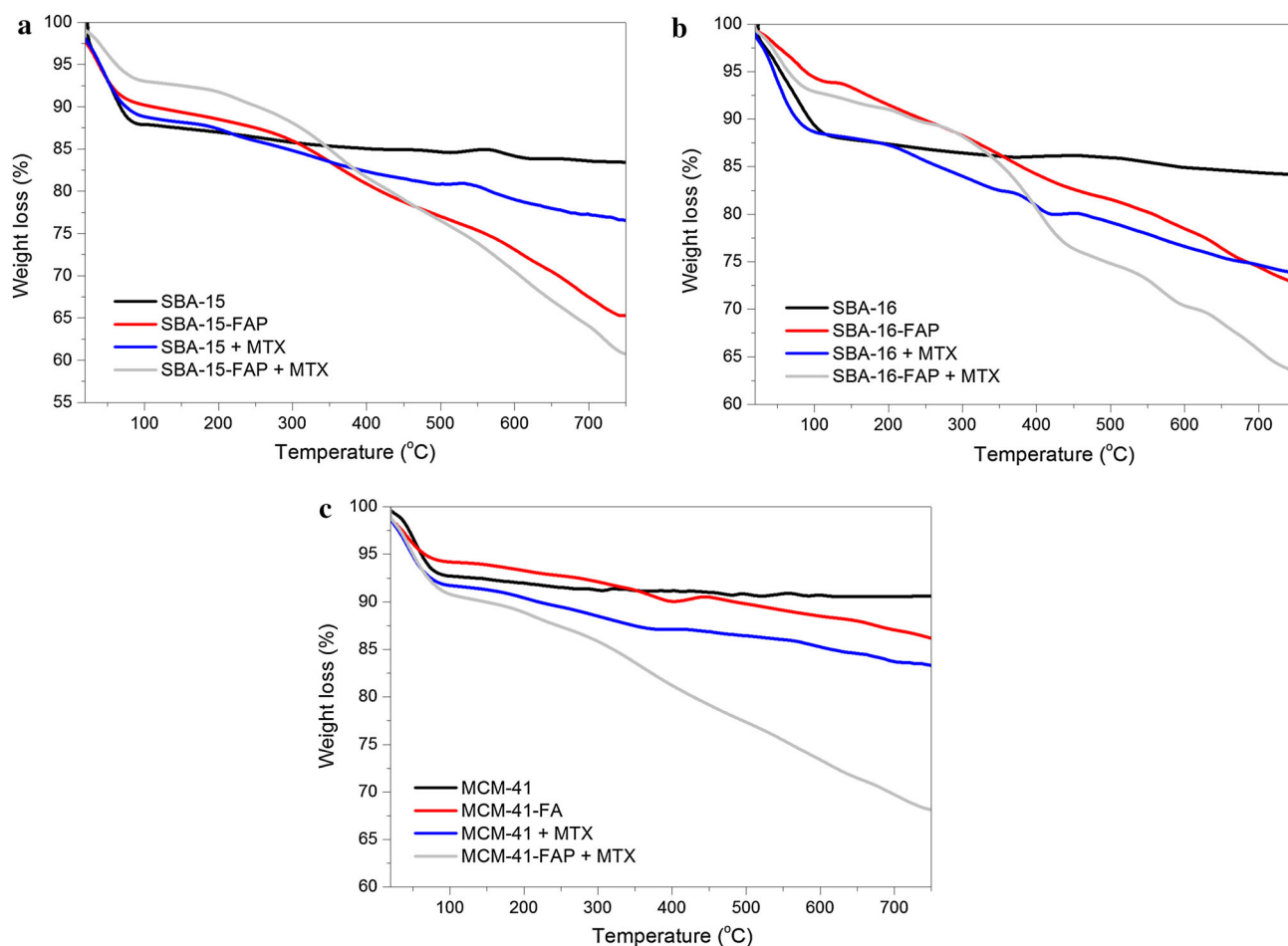| Samples	C (%)	ΔC (%)	H (%)	ΔH (%)	N (%)	ΔN (%)
SBA-15	0.1	–	1.6	–	–	–
SBA-15-FAP	15.4	15.3	2.6	1.0	6.4	6.4
SBA-15 + MTX	6.5	6.4	2.0	0.4	2.9	2.9
SBA-15-FAP + MTX	20.5	5.1	3.1	0.5	8.8	2.4
SBA-16	0.2	–	1.7	–	–	–
SBA-16-FAP	8.9	8.7	2.3	0.6	3.6	3.6
SBA-16 + MTX	6.7	6.5	2.2	0.5	3.0	3.0
SBA-16-FAP + MTX	14.2	5.3	3.2	0.9	6.2	2.6
MCM-41	0.3	–	0.5	–	–	–
MCM-41-FAP	6.9	6.6	2.6	2.1	2.7	2.7
MCM-41 + MTX	5.9	5.6	1.7	1.2	2.6	2.6
MCM-41-FAP + MTX	12.9	6.0	2.7	0.1	5.5	2.8

Fig. 5 TGA analysis of SBA-15 (**a**), SBA-16 (**b**) and MCM-41 (**c**) series

Table 2 Percentage of weight loss versus temperature

Sample	Weight loss (% w/w)		Residues > 650 °C (% w/w)
	20–150 °C	150–750 °C	
SBA-15	12.6	3.8	83.6
SBA-15-FAP	10.8	24.1	65.1
SBA-15 + MTX	12.0	11.4	76.6
SBA-15-FAP + MTX	7.5	31.8	60.7
SBA-16	12.1	3.7	84.2
SBA-16-FAP	6.4	20.6	73.0
SBA-16 + MTX	12.0	14.1	73.9
SBA-16-FAP + MTX	8.2	28.3	63.5
MCM-41	7.6	1.8	90.6
MCM-41-FAP	6.2	7.7	86.1
MCM-41 + MTX	8.7	7.9	83.4
MCM-41-FAP + MTX	10.2	21.7	68.1

confirms that the silica materials present an adequate thermal stability for the proposed application as directing drug carriers.

The TGA was also used to infer the amount of MTX incorporated in each sample, and the data found were again in accordance with elemental analysis. Regarding the bare

MSPs, the TGA curves showed a higher degree of MTX loading into SBA-16 (14.1 % w/w) than to SBA-15 (11.4 % w/w), which was higher than to MCM-41 (7.9 % w/w). Regarding the drug loading of the functionalized MSPs, the less functionalized silica, MCM-41-FAP, showed a higher value of drug loading (14 % w/w), while SBA-15-FAP and SBA-16-FAP presented lower values (7.0 and 7.7 % w/w, respectively).

3.6 Fourier transform infrared spectroscopy (FTIR)

Figure 6 shows the FTIR spectra for SBA-15, SBA-16 and MCM-41 series. All infrared spectra show the bands that are typical of mesoporous silica (SiO_2). The characteristic bands almost at 1080, 800 and 460 cm^{-1} corresponded to the anti-symmetric stretching (v_{as}), bending (δ) and out of plane of Si–O bonds, respectively. The vibrational band around 960 cm^{-1} is typical of the presence of silanol

groups (v Si–OH) commonly found in silica material. Additionally, all samples show a band around 1640 cm^{-1} which belongs to adsorbed water. The broadband centered at 3420 cm^{-1} is characteristic of hydroxyl stretching (v O–H) from silanol groups and from physically absorbed molecular water [46].

New bands in the spectra of SBA-15-FAP, SBA-16-FAP and MCM-41-FAP indicate the incorporation of the organic groups used in the functionalization step. The presence of a weak band around 2820–2940 cm^{-1} is attributed to (v C–H) of CH_2 groups of FA. The FTIR spectrum of these functionalized MSPs shows bands around 1510 cm^{-1}, belonging to the aromatic rings vibration (v C=C) of FA. The new band around 1640 cm^{-1} is assigned to the typical C=O vibration. The band from N–H stretching (at 3400 cm^{-1}) is superposed to the (v O–H) band. In the spectra of MSPs-FAP, bands at 1606–1539 cm^{-1} were assigned to the (v C=N), (δ N–H)
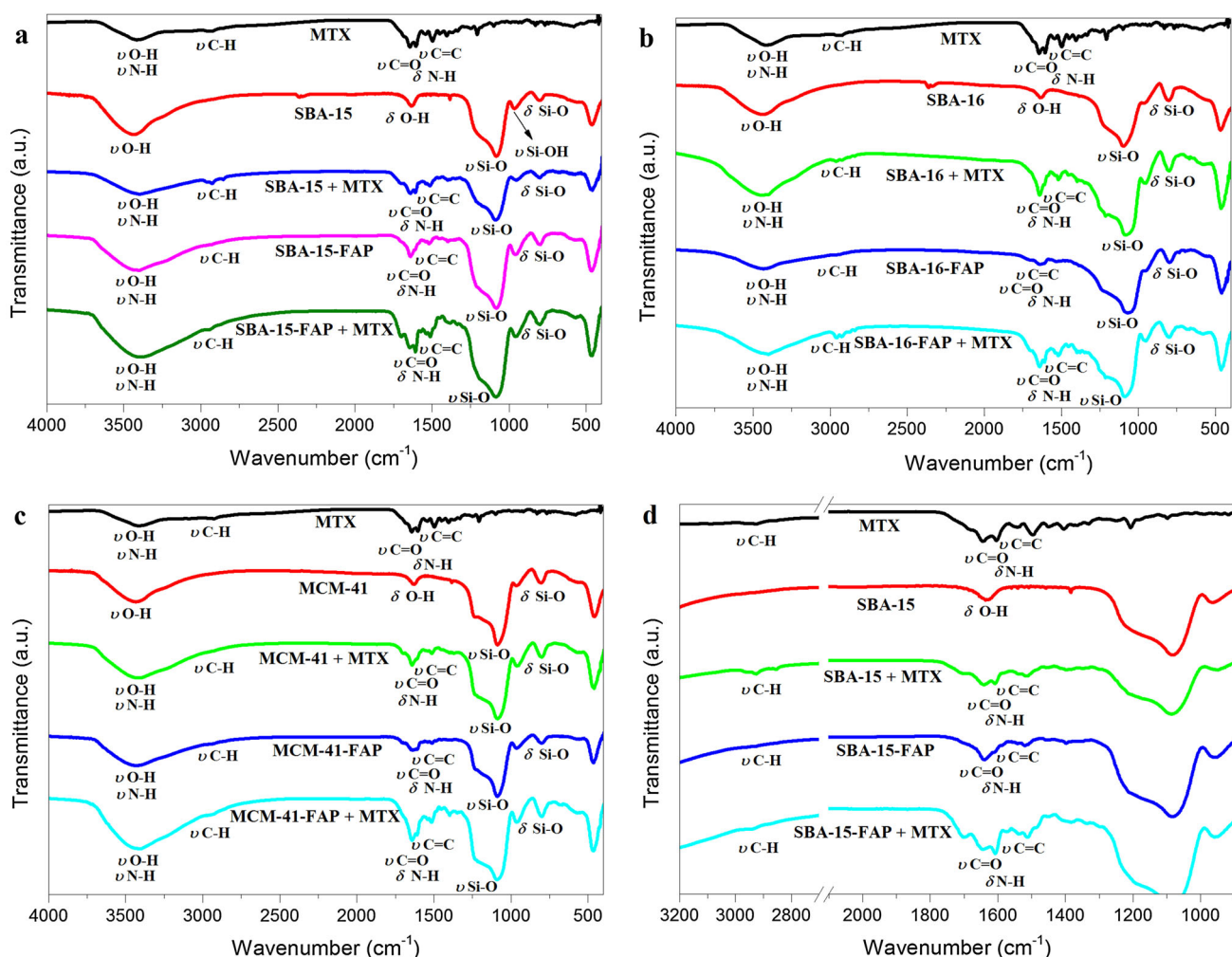

Fig. 6 FTIR spectra of MTX and SBA-15 series (a); MTX and SBA-16 series (b); MTX and MCM-41 series (c) and expansion of FTIR spectra of MTX and SBA-15 series (d)

and (δ O–H), that are also superposed. Therefore, the FTIR results demonstrate that FAP target ligand has been successfully grafted onto the MSPs' surface, which agrees with the results of CHN and TGA.

FTIR spectra of the MTX-loaded MSPs (Fig. 3) gave a direct demonstration that MTX is present in these matrices, since the spectra exhibit peaks that are characteristic of MTX drug molecules. The FTIR spectra of these samples show a broadband around 3400 cm^{-1}, assigned to (v N–H) from MTX and FA and to (v O–H) of silanol groups, water and the carboxylic acid groups from MTX and FA. When compared to the bare MSPs, after loading, the MTX characteristic absorption bands appear in the FTIR spectra of SBA-15 + MTX, SBA-16 + MTX and MCM-41 + MTX. The bands at 2940 cm^{-1} and 2850 cm^{-1} are attributed to the anti-symmetric and symmetric stretching vibration modes of the C–H bonds, respectively, from MTX CH$_2$ and CH$_3$ groups. The bands located between 1700 and 1465 cm^{-1} were assigned to the (v C=O), (v C=N), (v C=N) and (δ N–H) from MTX and FA and (δ O–H) from adsorbed water. As a result, the FTIR spectra demonstrate that MTX has been incorporated into the mesoporous matrices.

3.7 Zeta potential

Zeta potential measurements are used to characterize the residual surface charges of the particles. The mean zeta potential values of all materials are shown in Table 3. The mean zeta potential values of free SBA-15, SBA-16 and MCM-41 particles are −21.4, −23.8 and −24.9 mV, respectively. These results are due to the high amount of silanol groups on the silica surface [13]. After functionalization with FAP, the values lowered to −26.8, −25.1 and −25.9 mV, respectively. The change in the value could be attributed to the presence of carboxylic acid in FA structure. The biggest change in the potential value happened to the most functionalized sample, which is SBA-15-FAP, according to CHN and TGA analysis. These data confirm that FAP and not only APTES was successfully grafted to the silica surface, since silica modified with APTES usually

Table 3 Zeta potential analysis

Samples	ζ Potential $\pm$ SD (mV)[a]
SBA-15	−21.4 ± 0.7
SBA-15-FAP	−26.8 ± 0.5
SBA-16	−23.8 ± 0.7
SBA-16-FAP	−25.1 ± 1.0
MCM-41	−24.9 ± 0.2
MCM-41-FAP	−25.9 ± 0.6

[a] Measurement at a concentration of 0.05 mg/mL at pH 7,0

increases the values of zeta potential due to the presence of free amino groups [13, 41].

3.8 N$_2$ adsorption

The pore volume, pore size distribution and specific surface area were measured by N$_2$ adsorption–desorption. The most relevant values obtained from the isotherms (Fig. 7) are listed in Table 4. All bare MSPs display a type IV isotherm according to IUPAC classification, that are characteristic of mesoporous materials with a high surface area and a narrow pore size distribution [47].

Interestingly, the values of D_p calculated from N$_2$ desorption for the bare SBA-15, SBA-16 and MCM-41 matrices, i.e., 6.6, 3.4 and 3.1 nm, respectively, are close to those measured from the TEM images, which are 6.4, 3.5 and 2.4 nm, respectively.

The adsorption isotherm of SBA-15 shows a sharp increase in the amount of N$_2$ adsorbed at $0.7 < P/P_0 < 0.8$, corresponding to the capillary condensation of nitrogen inside the pores. Another important characteristic is the hysteresis loop of the isotherm, corresponding to type H1 hysteresis, which is typical for cylindrical pore geometry with a high degree of pore size uniformity [48].

The adsorption isotherm of SBA-16 shows an increase in N$_2$ volume adsorbed at $0.4 < P/P_0 < 0.6$, and contains asymmetrical and triangular adsorption and desorption branches. These characteristics can be assigned to systems with pore network connectivity and a pore-blocking effect, with an H2-type hysteresis loop.

The MCM-41 isotherm shows a sharp increase in the amount of N$_2$ adsorbed at $0.2 < P/P_0 < 0.3$. For this system, the pore filling is observed at pressures close to mono-multilayer formation, and the condensation in primary mesopores was not accompanied by hysteresis.

As expected, the introduction of the organic moiety (FAP) to the MSPs leads to a decrease in the surface area and in the pore volume (see Table 4). This decrease evidences that the pore wall is indeed covered by organic moieties and that the organic material is also located within the pores of the matrices. In addition, the pore diameter was reduced to SBA-15, did not change for SBA-16 and increased for MCM-41 after the functionalization.

3.9 Small-angle X-ray scattering (SAXS)

The pore structure was measured by small-angle X-ray scattering (SAXS). Figure 8 shows the SAXS patterns of pure and functionalized SBA-15, SBA-16 and MCM-41 samples.

Small-angle XRD of SBA-15 shows a well-resolved pattern with (100), (110) and (200) reflections at $2\theta = 0.90$, 1.56 and 1.81, respectively, characteristic of the
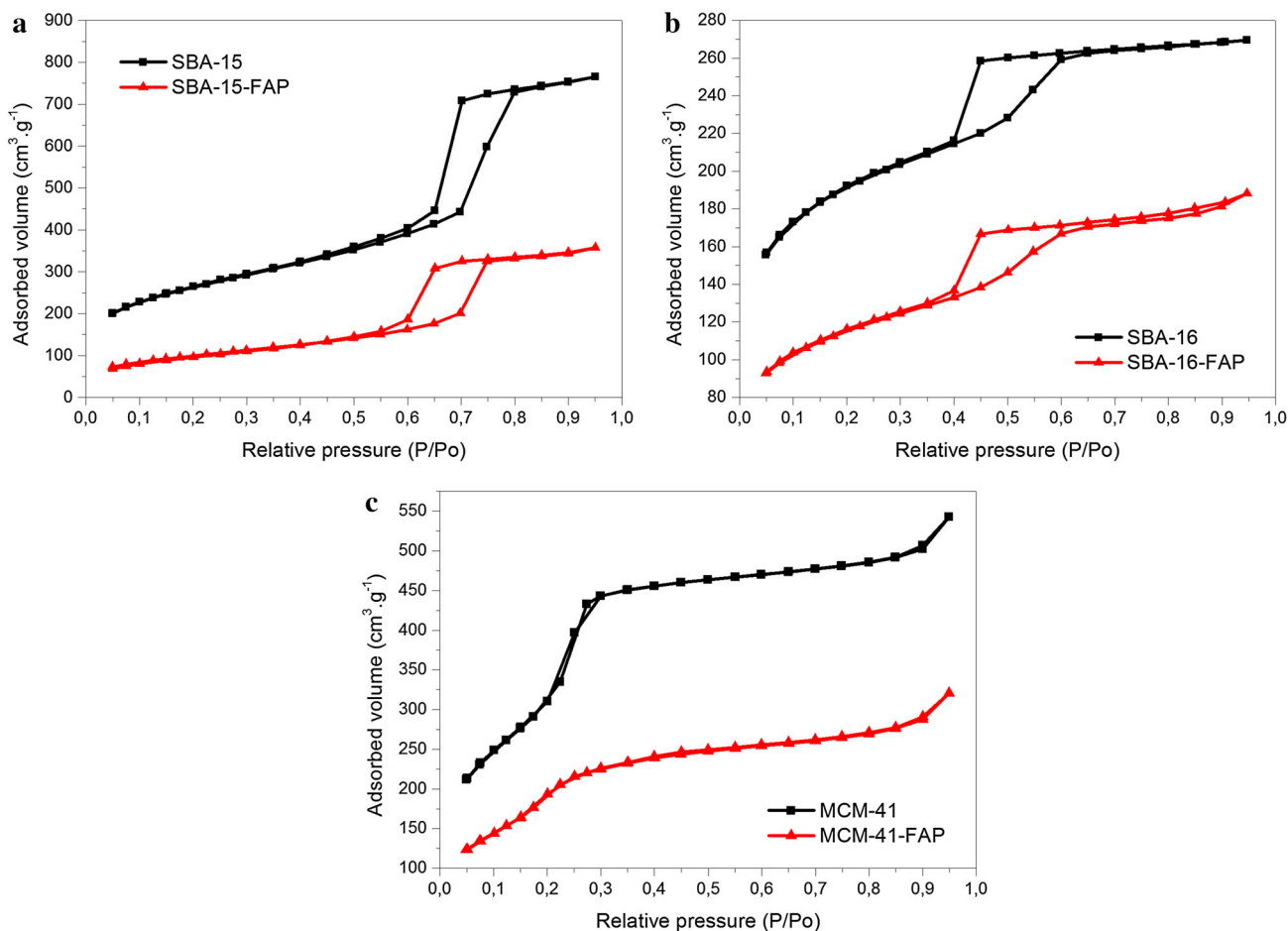
Fig. 7 N_2 adsorption isotherms of SBA-15 and SBA-15-FAP (**a**); SBA-16 and SBA-16-FAP (**b**); and MCM-41 and MCM-41-FAP (**c**) samples

Table 4 Structural parameters of SBA-15, SBA-15-FAP, SBA-16, SBA-16-FAP, MCM-41 and MCM-41-FAP samples

Samples	S_{BET} (m^{2}g^{-1})[a]	S_{BJH} (m^{2}g^{-1})[b]	V_p (cm^{3}g^{-1})[c]	D_p (nm)[d]
SBA-15	905.9	636.3	0.996	6.6
SBA-15-FAP	351.1	382.7	0.539	5.6
SBA-16	624.4	203.1	0.182	3.4
SBA-16-FAP	381.6	144.1	0.142	3.4
MCM-41	1517.7	111.3	0.158	3.1
MCM-41-FAP	741.7	67.4	0.112	3.4

[a] S_{BET} = surface area, calculated from BET method

[b] S_{BJH} = surface area, calculated from BJH method

[c] V_p = pore volume

[d] D_p = pore diameter, calculated from BJH method

hexagonal structure of silica SBA-15 [11]. The XRD patterns of the samples after functionalization showed no loss of structural ordering, with d_{100} spacing of 9.7 nm for both SBA-15 and SBA-15-FAP. In spite of a decrease in the intensity of the peaks for the functionalized sample and a

slight shift to right, it is clear that the host mesostructure has still ordered characteristic.

Small-angle XRD of SBA-16 shows a pattern with (110), (200) and (211) reflections at $2\theta = 0.92$, 1.31 and 1.54, respectively, characteristic of the 3D cubic mesoporous
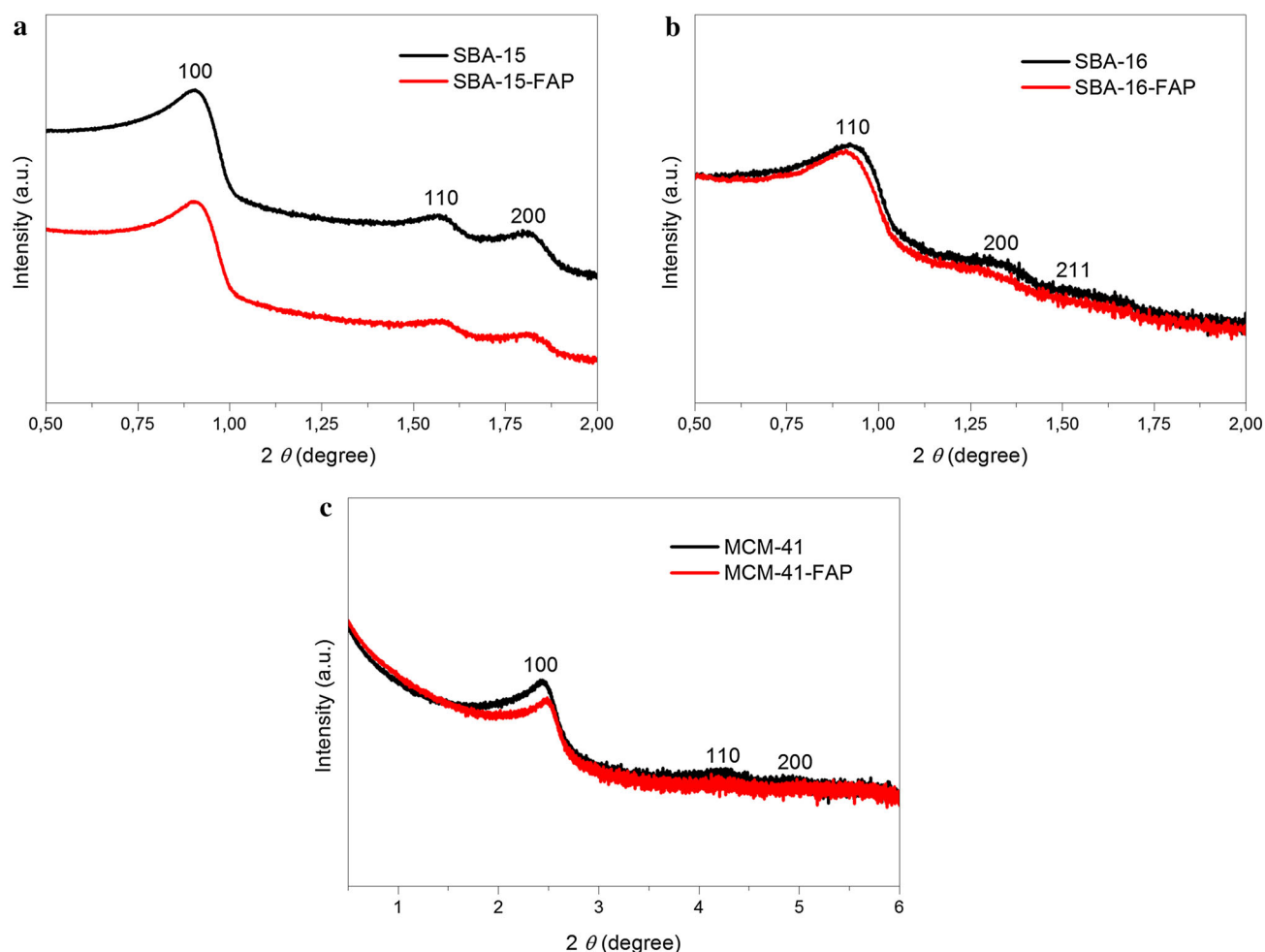
Fig. 8 Small-angle XRD patterns of **a** SBA-15 and SBA-15-FAP, **b** SBA-16 and SBA-16-FAP, and **c** MCM-41 and MCM-41-FAP samples

structure (*Im3m* plain group) with d_{110} spacing of 9.5 nm. This structure is characteristic of body-centered cubic [49], corresponding to a large unit cell parameter of $a_{110} = 13.5$ nm, which is in accordance with reported patterns of bare SBA-16 [10, 41]. The SAXS pattern of SBA-16-FAP exhibits peaks indexed as (110) and (200) which confirms the cubic array of modified material, showing d_{110} values of 9.7 nm and $a_0 = 13.7$ nm. The SAXS reflection intensities slightly decreased after the incorporation of organic groups, and it might be attributed to changes in the electron density between the walls of the pores and the voids.

Small-angle XRD of MCM-41 shows a pattern with (100), (110) and (200) reflections at $2\theta = 2.44$, 4.23 and 4.91, respectively, characteristic of the hexagonal structure of MCM-41 [50]. As observed to the other matrices, the SAXS pattern of MCM-41-FAP indicates that the functionalization of the pore wall did not affect the structural ordering. The d_{100} spacing for both MCM-41 and MCM-41-FAP was of 3.6 nm.

Table 5 Structural parameters of SBA-15, SBA-16, MCM-41 and its derivatives

Samples	$2\theta^a$	d (nm)^b	a (nm)^c	h (nm)^d
SBA-15	0.905	9.7	11.3	4.7
SBA-15-FAP	0.907	9.7	11.2	5.6
SBA-16	0.925	9.5	13.5	10.1
SBA-16-FAP	0.911	9.7	13.7	10.3
MCM-41	2.438	3.6	4.2	1.1
MCM-41-FAP	2.476	3.6	4.1	0.7

[a] θ = angle of incidence

[b] d = interplanar spacing, measurement at d_{100} for SBA-15 and MCM-41, and at d_{110} for SBA-16

[c] a = unit cell parameter

[d] h = wall thickness

When compared the wall thickness of the materials (see Table 5), it is clear that SBA-16 presents the thicker walls (10.1 nm), which is about the double thickness of SBA-15

(4.7) and 10 times thicker than MCM-41 (1.1 nm). This suggests a higher thermal and hydrothermal stability of SBA-16 when compared to the other two matrices [10].

3.10 X-ray photoelectron spectroscopy (XPS)

XPS results (Fig. 9a) show that the surface of bare MSPs is conformed only by Si, O and C. The presence of a low carbon concentration corresponds to surface adventitious carbon from environment contamination and some residual carbon of the organic template after the thermal treatment of the supports synthesis, as evidenced by the light asymmetry of the C 1s peak to high binding energy (BE) [32]. Regarding the functionalized samples (Fig. 9b), in addition to Si, O and C, it was detected only N from the organic moiety FAP, which evidences that the samples are free of contamination or residual reagents used during the samples preparation. The semiquantitative surface atomic concentration of the different samples, as obtained by XPS, is shown in Table 6.
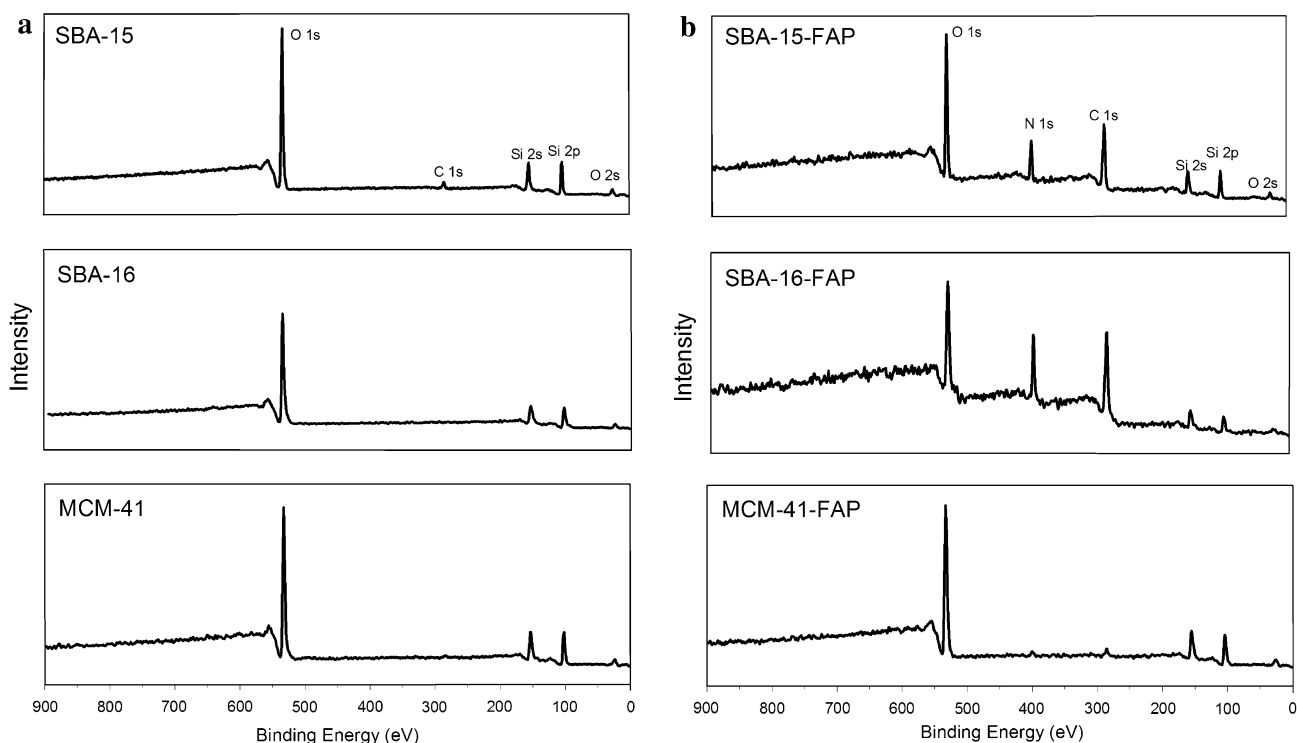

Fig. 9 XPS survey spectra of bare (a) and functionalized (b) MSPs

Table 6 Surface composition of the MSPs, as obtained by XPS

	Atomic concentration %				Atomic ratio		
	O 1s	C 1s	Si 2p	N 1s	O/Si	C/Si	N/Si
SBA-15	56.6	7.9	35.4	nd	1.6	0.2	nd
SBA-15-FAP	29.4	41.4	17.2	12.0	1.7	2.4	0.7
SBA-15 + MTX	52.2	12.9	32.1	2.8	1.6	0.4	0.1
SBA-15-FAP + MTX	25.4	46.2	12.2	16.2	2.1	3.8	1.3
SBA-16	59.3	2.4	38.2	nd	1.5	0.1	nd
SBA-16-FAP	23.0	49.3	11.0	16.8	2.1	4.5	1.5
SBA-16 + MTX	36.5	35.6	17.3	10.6	2.1	2.1	0.6
SBA-16-FAP + MTX	19.6	55.9	8.2	16.3	2.4	6.8	2.0
MCM41	59.1	3.0	37.9	nd	1.6	0.1	nd
MCM-41-FAP	53.0	10.1	34.2	2.6	1.5	0.3	0.1
MCM-41 + MTX	55.7	6.9	35.6	1.8	1.6	0.2	0.1
MCM-41-FAP + MTX	41.5	25.5	25.3	7.6	1.6	1.0	0.3

After folic acid grafting and drug loading, an increase in surface carbon and nitrogen content can be observed on all materials (Table 6), but it was more expressive for SBA-16, followed by SBA-15 matrix. The successive increase in the C/Si and N/Si atomic ratios for SBA-15-FAP and SBA-16-FAP, with or without MTX, in relation to bare MSPs, indicates a significant incorporation of organic material to their surface. In contrast, homologous MCM-41 samples show very low C/Si and N/Si atomic ratios, which evidences a poor surface functionalization.

It is important to mention although CHN and TGA techniques evidence that SBA-15 matrix presents a more efficient functionalization rate considering the highest amount organic material detected, the XPS analysis shows that the SBA-16 surface is the most functionalized, yielding higher concentrations of C and N. For a better understanding about the relative functionalization degree between the samples, two important parameters calculated from XPS results of the functionalized samples were considered: the surface functionalization parameter (SFP %), calculated from Eq. 1, and the type of functionalization (FX), calculated from Eq. 2:

$$SFP\% = C(1s)C_f\% + N(1s)N\% \qquad (1)$$

$$FX\% = X(1s)\%X/FSP\% \qquad (2)$$

where X is C_f or N, depending of the functionalization type, and the corrected carbon C_f is the carbon present in the functionalized sample surface less the carbon initially present in the bare MSP material.

A comparison of SFP % for the samples functionalized with the moiety FAP is shown in Fig. 10. Bar graph on Fig. 9 shows that the sample SBA-16-FAP presents a bigger %SFP (>60 %), followed by the SBA-15-FAP sample (46 %). This fact could be explained by the difference in textural properties of the MSPs matrices. SBA-15 matrix almost duplicates its values of V_p and D_p with respect to SBA-16 matrix (see Table 4), suggesting most functionalization could occur inside the pores where great part of the incorporate organic material cannot be detected by XPS, while in SBA-16 matrix most of functionalization occurs in the external surface area which would be higher due to its smaller D_p and V_p. When
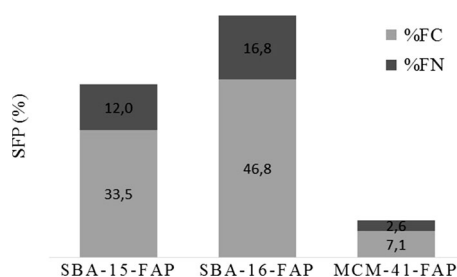
SBA-16 matrix is compared to MCM-41, where the values of D_p are similar, the difference in reactivity could be attributed to the presence of microporous connecting the mesoporous present only in SBA-16 matrix. These microporous might block partially the pore entrances during the grafting process and thus drive the silanization process to the external surface of SBA-16.

Figure 11 shows the deconvolutioned C 1s core level spectra of the functionalized MPSs (left panel) and the homologous loaded with MTX (right panel), which allowed to identify the different carbon species on surface. For all C 1s core level spectra can be observed a component around 282 eV with a differential charging effect in the sample (C*). This phenomenon is frequently observed in the Si, O and C photoelectron signals of some materials such as ceramics and zeolites, which have poor electrical conductivity [51, 52]. The functionalized MPSs SBA-15-FAP and SBA-16-FAP show a C 1s main component with BE at 284.6 eV, corresponding to C–C bonds assigned to the propyl chain in the FAP moiety, another component at 285.6 eV, attributed to the different C–N and C–O bonds present in the FAP, and two components at 286.7 and 288.5 eV as a consequence of the oxygenate functional groups C=O and COOH, respectively. In the case of the sample MCM-41-FAP, in addition to those components, it is observed an additional one around 292 eV, corresponding to residual CO_x species possibly from the matrix synthesis, due to a poor functionalization of the sample surface.

However, functionalized samples loaded with MTX present another C 1s component around 289 eV, suggesting, due to the high BE position, the presence of carbon with a new chemical environment created by the drug incorporation to surface that is possibly related to an electrostatic interaction of the carboxylate anion (COO$^-$) with the amino groups of MTX.

In the same way, deconvolution of the N 1s core level spectra (not shown) was also performed for the same group of samples. In all cases were observed spectral components around 397.7, 399.8 and 401.7 eV, corresponding to nitrogen atoms in the aromatic rings, amine groups (NH$_2$) and amide groups (NHCO), respectively, which are characteristic of the incorporated FAP. Furthermore, spectra from SBA-15-FAP and MCM-41-FAP samples show a low-intensity component above 403 eV that is attributed to protonated amine or imine groups, in agreement with the literature [53, 54]. Positions in BE and a quantification of the different C and N species on surface are resumed in Table 7.

When MSPs' surface is functionalized with FA, the C=O and COOH carbon species and NHCO nitrogen species are minority, indicating that carboxyl groups and adjacent amides are less exposed and therefore less detected at surface by XPS than C-N carbon type and
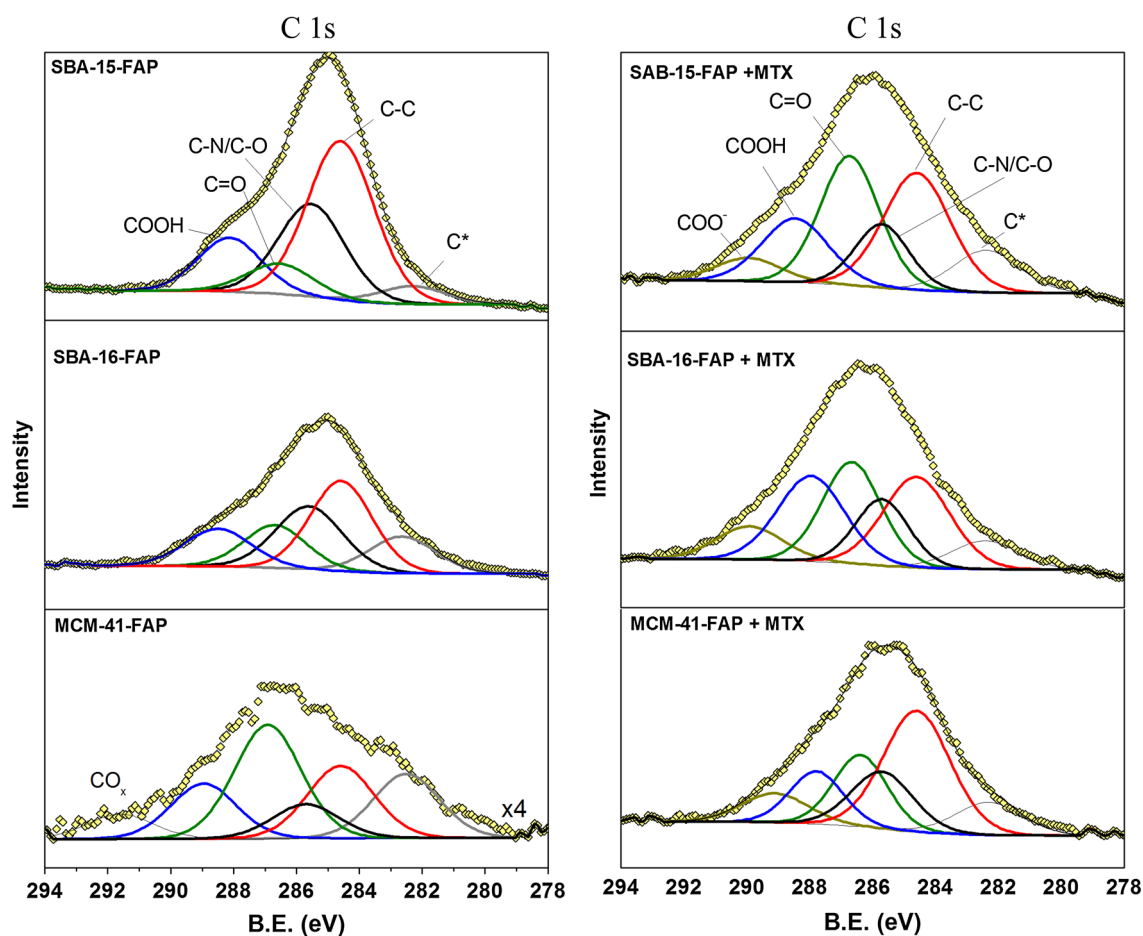

Fig. 10 Surface functionalization of MSPs with FAP

Fig. 11 C 1*s* core level spectra of the functionalized MSPs (*left panel*) and the homologous loaded with MTX (*right panel*)

nitrogen in amines. This fact would be in agreement with a possible perpendicular orientation of the FAP structure on the MPS surface, as illustrated in Fig. 4. In contrast, when the MTX is incorporated, there is a considerable increase in C=O, COOH and NHCO species besides the presence of the new carbon type at 289 eV, suggesting a more disperse arrangement of MTX molecules.

3.11 Loading efficiency

The elemental analysis was used to calculate the amount of MTX loaded into the MSPs. The percentage of the total amount of drug presented in the solution loaded into SBA-15, SBA-16 and MCM-41 matrices was 92.4, 95.2 and 80.8 %, respectively. For SBA-15-FAP, SBA-16-FAP and MCM-41-FAP, the drug load was about 74.2, 77.5 and 87.8 %, respectively.

When compared to their functionalized samples, non-functionalized SBA-15 and SBA-16 presented a higher incorporation rate of MTX. This behavior might be associated with more available spaces, due to a lack of

functionalizing agents. On the other hand, for MCM-41-FAP, the drug loading increased when compared to bare MCM-41. Similar results were found in studies with other drugs and functionalizing agents [10, 55]. The less functionalized system MCM-41-FAP incorporated more drug when compared to SBA-15-FAP and SBA-16-FAP, probably due to a higher free surface area available in the MSP to interact with MTX through hydrogen bonding or dipole–dipole interactions.

3.12 In vitro release kinetics study

The in vitro MTX release behavior from all MSPs was investigated as a function of time and is shown in Fig. 12. The drug release profile of unfunctionalized MSPs samples (Fig. 11a) in simulated body fluid shows two steps. Initially, for the approximately first 5 h, around 80 % of the loaded quantity was released. Specifically for SBA-15 and SBA-16 samples, it was observed a burst release effect in the first 30 min of assays (24 and 21 %, respectively). The initial burst release can be attributed to the immediate

Table 7 C and N species on the functionalized sample surface, as determined by XPS

Sample	C 1s			N 1s		
	Type	BE	At.%	Type	BE	At.%
SBA-15-FAP	C–C	284.6	47.7	$N_{in\ ring}$	397.9	9.5
	C–N/C–O	285.5	27.8	NH_2	399.7	85.7
	C=O	286.5	9.1	NHCO	401.6	2.3
	COOH	288.1	15.4	NH_3^+	403.2	2.5
SBA-15-FAP + MTX	C–C	284.6	31.7	$N_{in\ ring}$	397.7	12.4
	C–N/C–O	285.6	13.8	NH_2	399.8	34.7
	C=O	286.7	31.0	NHCO	401.5	53.0
	COOH	288.5	17.3			
	COO⁻	289.9	6.2			
SBA-16-FAP	C–C	284.6	37.3	$N_{in\ ring}$	397.7	22.4
	C–N/C–O	285.6	28.0	NH_2	399.6	67.0
	C=O	286.7	17.9	NHCO	401.3	10.6
	COOH	288.5	16.8			
SBA-16-FAP + MTX	C–C	284.6	25.8	$N_{in\ ring}$	397.6	9.0
	C–N/C–O	285.7	15.1	NH_2	399.8	41.1
	C=O	286.7	25.4	NH_2CO	401.6	49.9
	COOH	288.0	24.3			
	COO⁻	289.9	9.4			
MCM-41-FAP	C–C	284.6	24.1	$N_{in\ ring}$	397.5	15.7
	C–N/C–O	285.7	11.4	NH_2	399.8	35.9
	C=O	286.9	37.9	NH_2CO	401.7	38.5
	COOH	289.0	18.2	NH_3^+	404.2	9.9
	COx	291.6	8.3			
MCM-41-FAP + MTX	C–C	284.6	40.0	$N_{in\ ring}$	397.9	12.6
	C–N/C–O	285.7	17.4	NH_2	400.0	56.2
	C=O	286.4	19.0	NH_2CO	401.7	31.1
	COOH	287.8	14.0			
	COO⁻	289.1	9.7			
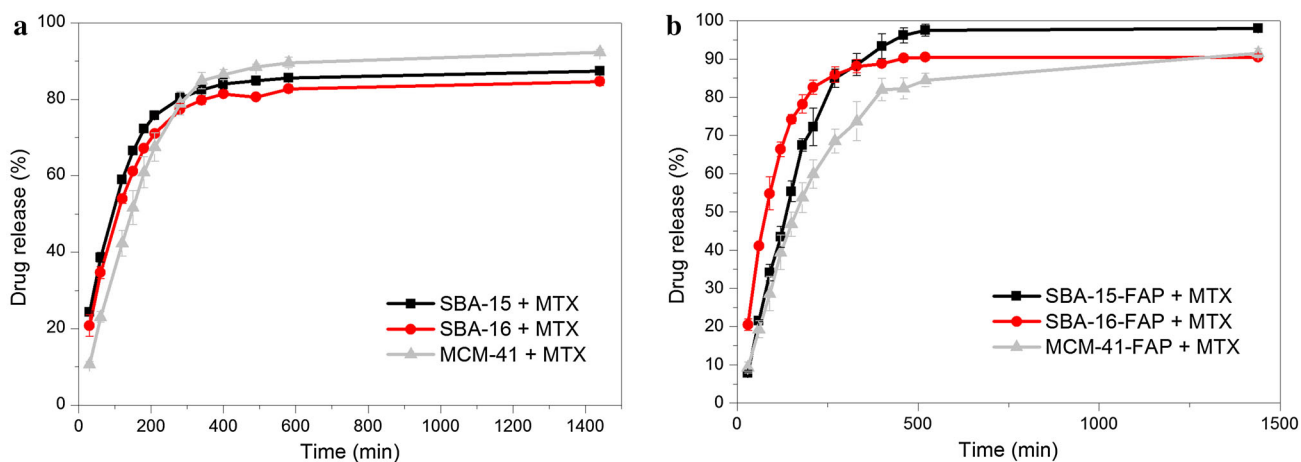
Fig. 12 Release profiles of MTX from SBA-15, SBA-16 and MCM-41 matrices (**a**) and from SBA-15-FAP, SBA-16-FAP and MCM-41-FAP (**b**)

dissolution and liberation of the portion of the drug located on the surface or near the external pores of the surface. It could also be observed that MCM-41 matrix released a smaller percentage of MTX than did MCM-41-FAP at 5 h (10 %), but the overall release was almost the same (∼90 %) after 24 h.

The second step represents a very slow and extended drug release which might be explained due to MTX interactions in the inner of microporous spaces [8].

According to the drug release profiles of bare MSPs, there was no significant difference between the three matrices, except that the initial burst release of MTX by MCM-41 was slower than it was for SBA-15 and SBA-16 matrices. This can be explained due to the lower percentage of MTX adsorbed on the external surface of MCM-41, as can be seen by the XPS results. The MTX located on the external surface can be released more easily, since they have fewer interactions with the silanol groups from the surface, and they also have less mechanical barriers to leave the pores.

On the other hand, the drug release profiles of the functionalized samples showed more significant differences. For example, SBA-16-FAP exhibited a pronounced initial burst release of ∼ 20 % (at 30 min), which is in accordance with the high amount of drug loaded on the surface, as demonstrated by XPS, while SBA-15-FAP and MCM-41-FAP presented smaller amount of release in this period (around 8 % of the loaded quantity for both samples). For the SBA-15-FAP sample, approximately 100 % of the drug was released at ∼500 min, which was greater than the pure sample.

In order to investigate the release mechanism of MTX from the MSPs, the data were fitted to the Korsmeyer–Peppas model [6, 56, 57], applying Eq. 3:

$$\frac{Mt}{M\infty} = Kt^n \qquad (3)$$

where $Mt/M\infty$ is the fraction of drug released at time t, K is a kinetic constant characteristic of the drug-carrier system, and n is the release index, indicative of the mechanism of drug release [56]. If $n = 0.45$, it represents Case I or Fickian diffusion mechanism. For $0.45 < n < 0.89$, anomalous behavior or non-Fickian diffusion is observed, while $n = 0.89$ provides Case II transport mechanism, which characterizes zero-order release behavior. Values of n higher than 0.89 mean a Super Case II transport [57, 58]. This model is generally used to analyze the release of which mechanism is not well known or when more than one type of release phenomena is involved.

The parameters of Eq. 3 can be obtained from Eq. 4. The $\ln(Mt/M\infty)$ was plotted as a function of $\ln(\text{time})$ (not shown), and a good regression coefficient R^2 was obtained until approximately 70 % of MTX release.

Table 8 Release parameters of MTX from all materials

Samples	Korsmeyer–Peppas			Transport mechanism
	R^2	n value	K	
SBA-15	0.9947	0.55	4.12	Anomalous
SBA-15-FAP	0.9944	0.98	0.39	Super Case II
SBA-16	0.9918	0.58	3.21	Anomalous
SBA-16-FAP	0.9906	0.65	2.86	Anomalous
MCM-41	0.9900	0.82	0.82	Anomalous
MCM-41-FAP	0.9892	0.85	0.61	Anomalous

$$\ln\left(\frac{Mt}{M\infty}\right) = \ln K + n \ln t \qquad (4)$$

As can be observed from Table 8, the release exponent is similar for SBA-15 and SBA-16 structures (0.55 and 0.58, respectively), but the exponents for these modified structures are 0.98 and 0.65, respectively. Therefore, it is believed that MTX release from as-prepared samples approximately follows Fick's law, SBA-16-FAP system follows anomalous non-Fick's transport, and SBA-15-FAP system follows a Super Case II release mechanism, which was close to a linear zero-order type of release ($n = 0.98$), typical for slow-dissolving drugs. Comparing the results obtained for MCM-41 systems, both samples present release exponent values around 0.85, that are in-between the extreme, the so-called anomalous transport, indicating an overlapping of different mechanisms, including drug diffusion.

The kinetic constant K, that is associated with the drug release rate, was estimated by using Eq. 4 (Table 8). The experiments have demonstrated a significant effect on the kinetic constants calculated by the release of MTX by the different systems, since the K values range from 4.12 to 0.39. In general, all the functionalized MSPs showed K values smaller than the corresponding bare materials, suggesting a stronger interaction between MTX and the FAP group when compared to the silanol groups, probably through electrostatic interactions. A faster release kinetic is evidenced for bare SBA-15 ($K = 4.12$), and it is probably related to its bigger value of V_p and D_p (0.996 cm^3 g^{-1} and 6.6 nm, respectively) and pore system ($p6mm$ symmetry), which facilitates the diffusion process [36, 59]. Among the functionalized samples, SBA-15-FAP presents slower drug release ($K = 0.39$) compared to the other samples. This significant difference in kinetics may be explained by the differences in the functionalization rate. For example, in the more functionalized MSP, SBA-15-FAP, the MTX molecules might be more strongly interacting with the FAP groups through electrostatic interactions, hydrogen bonds and dipole–dipole interactions than to the silanol groups

from silica. This observation is in agreement with the kinetic model used to fit the release pattern, where the rate-controlling step is close to linear zero-order type ($n = 0.98$) which is typical for slow-dissolving drugs.

On the other hand, the MCM-41 and MCM-41-FAP samples, that possess the same pore system but with smaller V_p and D_p (0.158 cm^3 g^{-1} and 3.1 nm, respectively) than SBA-15 and that is less functionalized, showed a lower value of kinetic constants ($K = 0.82$ and $K = 0.61$, respectively). SBA-16 matrix is better to be directly compared to MCM-41 matrix, since they present close values of V_p and D_p (0.182 cm^3 g^{-1} and 3.4 nm, respectively, for SBA-16). In this case, the main factor to influence the kinetics profile is the pore symmetry, that is 3D cubic for SBA-16 (*Im3m* group), while 2D hexagonal for MCM-41. Many studies have proven that 3D systems with interconnected pores provide easier and faster diffusion process than unconnected pore systems [2, 36, 60].

Drug release process is usually complex and might be governed by diffusion, erosion and other mechanisms [22, 58]; however, the results showed above may provide a better understanding of the MTX release kinetics from the studied matrices.

4 Conclusions

In this current work, the surface functionalization of mesoporous silica SBA-15, SBA-16 and MCM-41 with folic acid was achieved using a one-pot process by post-synthesis grafting. The adequate combination of different characterization techniques allowed us to show the functional group *N*-folate-3-aminopropyl (FAP) was linked on the surface of MNPs samples, although the degree of functionalization differs depending on their structural characteristic. The presence of these organic groups was also evaluated by XPS, a surface-sensitive technique, which confirms the influence of the difference in textural properties of the MSPs matrices in the chemical modification process and suggests the link of hydroxyl groups to organic groups on silica surface. The modification of these materials' surface with FAP groups leads toward formation of carriers systems with potential use for the adsorption and in vitro release of MTX as targeted drug delivery. This study showed that the values of the kinetic constants K for the diverse systems presented significant differences. On the other hand, there were no distinguishable changes in the drug loading between the three different kinds of mesoporous silica, although they present distinct textural and structural properties. This result is interesting since the presence of organic moieties anchored into silica surface could be used to give a new property to the mesoporous silica, such as a directing agent, without losing its drug-

loading efficiency. This study suggests that these systems could be used as carriers for drug delivery and now some in vitro experiments with cancer and normal cells should be conducted in order to evaluate their biocompatibility and selectivity to cancer cells.

References

1. Safari J, Zarnegar Z (2014) Advanced drug delivery systems: nanotechnology of health design A review. J Saudi Chem Soc 18:85–99. doi:10.1016/j.jscs.2012.12.009
2. Yang P, Gai S, Lin J (2012) Functionalized mesoporous silica materials for controlled drug delivery. Chem Soc Rev 41:3679–3698. doi:10.1039/c2cs15308d
3. Slowing II, Vivero-Escoto JL, Wu C-W, Lin VS-Y (2008) Mesoporous silica nanoparticles as controlled release drug delivery and gene transfection carriers. Adv Drug Deliv Rev 60:1278–1288. doi:10.1016/j.addr.2008.03.012
4. Kwon S, Singh RK, Perez RA et al (2013) Silica-based mesoporous nanoparticles for controlled drug delivery. J Tissue Eng 4:2041731413503357. doi:10.1177/2041731413503357
5. Mamaeva V, Sahlgren C, Lindén M (2013) Mesoporous silica nanoparticles in medicine—recent advances. Adv Drug Deliv Rev 65:689–702. doi:10.1016/j.addr.2012.07.018
6. Wang S (2009) Ordered mesoporous materials for drug delivery. Microporous Mesoporous Mater 117:1–9. doi:10.1016/j.micromeso.2008.07.002
7. Roggers R, Kanvinde S, Boonsith S, Oupický D (2014) The practicality of mesoporous silica nanoparticles as drug delivery devices and progress toward this goal. AAPS PharmSciTech 15:1163–1171. doi:10.1208/s12249-014-0142-7
8. Moritz M, Geszke-Moritz M (2015) Mesoporous materials as multifunctional tools in biosciences: principles and applications. Mater Sci Eng C 49:114–151. doi:10.1016/j.msec.2014.12.079
9. Moritz M, Łaniecki M (2011) Modified SBA-15 as the carrier for metoprolol and papaverine: adsorption and release study. J Solid State Chem 184:1761–1767. doi:10.1016/j.jssc.2011.05.015
10. Andrade GF, Soares DCF, Almeida RKDS, Sousa EMB (2012) Mesoporous silica SBA-16 functionalized with alkoxysilane groups: preparation, characterization, and release profile study. J Nanomater 2012:1–10. doi:10.1155/2012/816496
11. Doadrio JC, Sousa EMB, Izquierdo-Barba I et al (2006) Functionalization of mesoporous materials with long alkyl chains as a strategy for controlling drug delivery pattern. J Mater Chem 16:462. doi:10.1039/b510101h
12. Alexa IF, Pastravanu CG, Ignat M, Popovici E (2013) A comparative study on long-term MTX controlled release from intercalated nanocomposites for nanomedicine applications. Colloids Surf B Biointerfaces 106:135–139. doi:10.1016/j.colsurfb.2013.01.022
13. Pang J, Zhao L, Zhang L et al (2013) Folate-conjugated hybrid SBA-15 particles for targeted anticancer drug delivery. J Colloid Interface Sci 395:31–39
14. Thomas MJK, Slipper I, Walunj A et al (2010) Inclusion of poorly soluble drugs in highly ordered mesoporous silica

nanoparticles. Int J Pharm 387:272–277. doi:10.1016/j.ijpharm.2009.12.023

15. Treccani L, Yvonne Klein T, Meder F et al (2013) Functionalized ceramics for biomedical, biotechnological and environmental applications. Acta Biomater 9:7115–7150. doi:10.1016/j.actbio.2013.03.036

16. Knežević NŽ, Durand J-O (2015) Targeted treatment of cancer with nanotherapeutics based on mesoporous silica nanoparticles. ChemPlusChem 80:26–36. doi:10.1002/cplu.201402369

17. Sudimack J, Lee RJ (2000) Targeted drug delivery via the folate receptor. Adv Drug Deliv Rev 41:147–162. doi:10.1016/S0169-409X(99)00062-9

18. Fan J, Fang G, Wang X et al (2011) Targeted anticancer prodrug with mesoporous silica nanoparticles as vehicles. Nanotechnology 22:455102. doi:10.1088/0957-4484/22/45/455102

19. Rosenholm JM, Meinander A, Peuhu E et al (2009) Targeting of porous hybrid silica nanoparticles to cancer cells. ACS Nano 3:197–206. doi:10.1021/nn800781r

20. Lu J, Li Z, Zink JI, Tamanoi F (2012) In vivo tumor suppression efficacy of mesoporous silica nanoparticles-based drug-delivery system: enhanced efficacy by folate modification. Nanomedicine 8:212–220. doi:10.1016/j.nano.2011.06.002

21. Lu Y, Low PS (2012) Folate-mediated delivery of macromolecular anticancer therapeutic agents. Adv Drug Deliv Rev 64:342–352. doi:10.1016/j.addr.2012.09.020

22. Pang J, Zhao L, Zhang L et al (2013) Folate-conjugated hybrid SBA-15 particles for targeted anticancer drug delivery. J Colloid Interface Sci 395:31–39. doi:10.1016/j.jcis.2012.12.016

23. Nzila A, Okombo J, Becker RP et al (2010) Anticancer agents against malaria: time to revisit? Trends Parasitol 26:125–129. doi:10.1016/j.pt.2009.12.002

24. Kozub P, Simaljakova M (2011) Systemic therapy of psoriasis: methotrexate. Bratisl Lek Listy 112:390–394

25. Vadia N, Rajput S (2012) Study on formulation variables of methotrexate loaded mesoporous MCM-41 nanoparticles for dissolution enhancement. Eur J Pharm Sci 45:8–18. doi:10.1016/j.ejps.2011.10.016

26. Barberá A, Lorenzo N, Domínguez C (2012) Current treatment of rheumatoid arthritis. Perspectives for the development of antigen-specific therapies. Biotecnología Aplicada 29:146–154

27. Zhao D (1998) Triblock copolymer syntheses of mesoporous silica with periodic 50 to 300 angstrom pores. Science 279:548–552. doi:10.1126/science.279.5350.548

28. Zhao D, Huo Q, Feng J et al (1998) Nonionic triblock and star diblock copolymer and oligomeric surfactant syntheses of highly ordered, hydrothermally stable, mesoporous silica structures. J Am Chem Soc 7863:6024–6036

29. Slowing II, Vivero-Escoto JL, Trewyn BG, Lin VS-Y (2010) Mesoporous silica nanoparticles: structural design and applications. J Mater Chem 20:7924. doi:10.1039/c0jm00554a

30. Smith JL, Herman RG, Terenna CR et al (2004) Sorption of nitrogen bases and XPS study of mesoporous solid acid SBA-15. J Phys Chem A 108:39–46. doi:10.1021/jp0305990

31. Hernández-Morales V, Nava R, Acosta-Silva YJ et al (2012) Adsorption of lead (II) on SBA-15 mesoporous molecular sieve functionalized with -NH2 groups. Microporous Mesoporous Mater 160:133–142. doi:10.1016/j.micromeso.2012.05.004

32. Ferraris S, Perero S, Vern E et al (2011) Surface functionalization of Ag–nanoclusters–silica composite films for biosensing. Mater Chem Phys 130:1307–1316. doi:10.1016/j.matchemphys.2011.09.019

33. Zhao X, Lu G, Hu X (2000) Characterization of the structural and surface properties of chemically modified MCM-41 material. Microporous Mesoporous Mater 41:37–47. doi:10.1016/S1387-1811(00)00262-6

34. Vrancken K, Possemiers K, Van Der Voort P, Vansant E (1995) Surface modification of silica gels with aminoorganosilanes. Colloids Surf A Physicochem Eng Asp 98:235–241. doi:10.1016/0927-7757(95)03119-X

35. Hanu LG, Hanu AM, Popovici E, Timpu D (2004) Nanosiliceous matrix for drug incapsulation. Romanian J Phys 49:817–822

36. Andersson J, Rosenholm J, Areva S, Lindén M (2004) Influences of material characteristics on ibuprofen drug loading and release profiles from ordered micro- and mesoporous silica matrices. Chem Mater 16:4160–4167. doi:10.1021/cm0401490

37. Balas F, Manzano M, Horcajada P, Vallet-Regi M (2006) Confinement and controlled release of bisphosphonates on ordered mesoporous silica-based materials. J Am Chem Soc 128:8116–8117. doi:10.1021/ja062286z

38. Qu F, Zhu G, Lin H et al (2006) A controlled release of ibuprofen by systematically tailoring the morphology of mesoporous silica materials. J Solid State Chem 179:2027–2035. doi:10.1016/j.jssc.2006.04.002

39. De Sousa A, de Souza KC, Leite PM da S, et al (2014) A dual-functional [SBA-15/Fe3O4/P(N-iPAAm)] hybrid system as a potential nanoplatform for biomedical application. doi:10.1039/c2ce25395j

40. Kleitz F, Kim TW, Ryoo R (2006) Phase domain of the cubic Im3⁻m mesoporous silica in the EO 106PO70EO106-butanol-H2O system. Langmuir 22:440–445. doi:10.1021/la052047+

41. Andrade GF, Soares DCF, dos Santos RG, Sousa EMB (2013) Mesoporous silica SBA-16 nanoparticles: synthesis, physico-chemical characterization, release profile, and in vitro cytocompatibility studies. Microporous Mesoporous Mater 168:102–110. doi:10.1016/j.micromeso.2012.09.034

42. Kim JM, Chang SM, Kong SM et al (2009) Control of hydroxyl group content in silica particle synthesized by the sol-precipitation process. Ceram Int 35:1015–1019. doi:10.1016/j.ceramint.2008.04.011

43. Jaroniec C, Gilpin R, Jaroniec M (1997) Adsorption and thermogravimetric studies of silica-based amide bonded phases. J Phys 44242:6861–6866. doi:10.1021/jp964002a

44. Vora A, Riga A, Dollimore D, Alexander KS (2002) Thermal stability of folic acid. Thermochim Acta 392–393:209–220. doi:10.1016/S0040-6031(02)00103-X

45. El-Wahed MGA, Refat MS, El-Megharbel SM (2008) Synthesis, spectroscopic and thermal characterization of some transition metal complexes of folic acid. Spectrochim Acta Part A Mol Biomol Spectrosc 70:916–922. doi:10.1016/j.saa.2007.10.008

46. Stuart B (2004) Infrared spectroscopy: fundamentals and applications. Wiley, Sydney

47. Sing KSW (1985) Reporting physisorption data for gas/solid systems with special reference to the determination of surface area and porosity (recommendations 1984). Pure Appl Chem 57:603–619. doi:10.1351/pac198557040603

48. Kruk M, Jaroniec M (2001) Gas adsorption characterization of ordered organic–inorganic nanocomposite materials. Chem Mater 13:3169–3183. doi:10.1021/cm0101069

49. Sakamoto Y, Kaneda M, Terasaki O et al (2000) Direct imaging of the pores and cages of three-dimensional mesoporous materials. Nature 408:449–453. doi:10.1038/35044040

50. Beck JS, Vartuli JC, Roth WJ et al (1992) A new family of mesoporous molecular sieves prepared with liquid crystal templates. J Am Chem Soc. doi:10.1021/ja00053a020

51. Kaliaguine S (1996) Serge Kaliaguine D6partement de g6nie chimique, Universit~Laval, Ste-Foy, Qu6bec, G1K 7P4, Canada 1. 102:191–230

52. Ambrogi V, Donnadio A, Pietrella D et al (2014) Chitosan films containing mesoporous SBA-15 supported silver nanoparticles for wound dressing. J Mater Chem B 2:6054. doi:10.1039/C4TB00927D

53. Lindberg B, Maripuu R, Siegbahn K et al (1983) ESCA Studies of heparinized and related surfaces. J Colloid Interface Sci 95:308–321. doi:10.1016/0021-9797(83)90190-X

54. Kallury KMR, Macdonald PM, Thompson M (1994) Effect of surface water and base catalysis on the silanization of silica by (aminopropyl) alkoxysilanes studied by X-ray photoelectron spectroscopy and 13C cross-polarization/magic angle spinning nuclear magnetic resonance. Langmuir 10:492–499

55. Manzano M, Aina V, Areán CO et al (2008) Studies on MCM-41 mesoporous silica for drug delivery: effect of particle morphology and amine functionalization. Chem Eng J 137:30–37. doi:10.1016/j.cej.2007.07.078

56. Korsmeyer RW, Gurny R, Doelker E et al (1983) Mechanisms of solute release from porous hydrophilic polymers. Int J Pharm 15:25–35. doi:10.1016/0378-5173(83)90064-9

57. Costa P, Sousa Lobo JM (2001) Modeling and comparison of dissolution profiles. Eur J Pharm Sci 13:123–133. doi:10.1016/S0928-0987(01)00095-1

58. Kumar S, Singh AK, Prajapati SK, Singh VK (2012) Formulation and evaluation of once daily sustained release matrix tablets of aceclofenac using natural gums. J Drug Deliv Ther 2:16–24

59. Horcajada P, Rámila A, Pérez-Pariente J, Vallet-Regí M (2004) Influence of pore size of MCM-41 matrices on drug delivery rate. Microporous Mesoporous Mater 68:105–109. doi:10.1016/j.micromeso.2003.12.012

60. Izquierdo-Barba I, Sousa E, Doadrio JC et al (2009) Influence of mesoporous structure type on the controlled delivery of drugs: release of ibuprofen from MCM-48, SBA-15 and functionalized SBA-15. J Sol Gel Sci Technol 50:421–429. doi:10.1007/s10971-009-1932-3